Drained Bearing Capacity of Shallowly Embedded Pipelines

Joe G. Tom, A.M.ASCE[1] and David J. White[2]

[1]Centre for Offshore Foundation Systems, The University of Western Australia, Crawley 6009, WA, Australia. E-mail: joe.tom@uwa.edu.au

[2]Faculty of Engineering and Physical Sciences, University of Southampton, Southampton SO17 1BJ, United Kingdom.

ABSTRACT

This study establishes the drained bearing capacity of pipelines embedded up to one diameter into the seabed subject to combined vertical-horizontal loading. Non-associated flow finite element analyses are used to calculate the peak breakout resistance in a non-associated flow, frictional Mohr-Coulomb seabed. Critical state friction angles and dilation angles ranging from 25^o to 45^o and 0^o to 25^o, respectively, are considered. Analytical expressions have been fitted to the results as a function of embedment depth and soil properties, and compare well with experimental measurements from previous studies. The horizontal bearing capacity at small vertical loads is also predicted well via upper bound limit analysis using the Davis reduced friction angle that accounts for the peak friction and dilation angles. The analytical relationships presented in this study provide simple predictive tools for estimating the bearing capacity of pipelines on free-drained sandy seabeds. These fill a void in knowledge for pipeline stability and buckling design by providing general relationships between drained strength properties and pipeline bearing capacity. The insight gained through the good comparison with limit analysis techniques also gives confidence in the use of simple numerical techniques to predict the bearing capacity of pipelines for more wide-ranging (i.e. non-flat) seabed topography.

Keywords: Pipelines, bearing capacity

INTRODUCTION

The bearing capacity of subsea pipelines is a primary input for many design areas, including on-bottom stability and global buckling management. This paper is concerned with the drained bearing capacity of a subsea pipeline that is subjected to combinations of vertical and horizontal loading.

If a pipeline has insufficient geotechnical bearing capacity (or breakout resistance) to resist externally-applied environmental or other operational loads then significant movements may occur, jeopardising the integrity of the pipeline. Accurate assessment of the available resistance can lead to significant cost savings in capital expenditure for offshore projects if pipeline stabilisation measures can be optimised. High temperature and pressure oil and gas pipelines also undergo operational expansions during start-up and shutdown cycles, which must be safely accommodated to prevent pipeline damage. Global buckling design is particularly complicated because the geotechnical resistance must be bracketed: a conservative design may rely on either an upper or lower estimate depending on the context.

Pipeline bearing capacity is further complicated by the fact that either drained or undrained (or intermediate, partially drained) conditions can prevail during breakout. Drainage conditions depend on the consolidation properties of the soil, the rate and duration of loading and the embedment condition of the pipeline. Drainage affects both the shear strength of the soil as well as the kinematics at failure. During undrained loading volume change does not occur, and associated flow conditions prevail at failure. The resulting volumetric and kinematic constraints allow exact bearing capacity solutions to be bounded using limit theorems (Martin and White 2012). Under drained conditions volume change may occur at failure, and the soil strength is controlled by friction. For drained failure the mobilised shear strength varies throughout the failure mechanism, and the resulting kinematics are complicated by the occurrence of volumetric strains due to non-associated flow.

The current understanding of drained pipeline bearing capacity is based primarily on experimental studies. Verley and Sotberg (1994) summarised three datasets from testing on silica sands and proposed a power law relationship to calculate the peak breakout resistance, which is a function of the applied vertical load and the pipeline embedment:

$$\begin{aligned} \frac{H}{\gamma' D^2} &= \left(5.0 - 0.15\frac{\gamma' D^2}{V}\right)\left(\frac{w}{D}\right)^{1.25} + 0.6\frac{V}{\gamma' D^2} \qquad \text{for } \frac{\gamma' D^2}{V} \leq 20 \\ \frac{H}{\gamma' D^2} &= 2.0\left(\frac{w}{D}\right)^{1.25} + 0.6\frac{V}{\gamma' D^2} \qquad \text{for } \frac{\gamma' D^2}{V} > 20 \end{aligned} \tag{1}$$

where H and V are the vertical and horizontal loads (per unit length) at failure, γ' is the soil effective unit weight, D is the pipeline diameter, w/D is the normalised pipeline embedment measured from the pipeline invert (Figure 1). This method was based on tests conducted for embedments less than 35% of the pipeline diameter and no data was provided regarding the friction angle or other strength characteristics of the materials tested.

Zhang (2001) and Zhang et al. (2002) describe centrifuge tests on pipelines embedded in calcareous sands. Based on these results, Zhang et al. (2002) presented a plasticity-based macro-element model for calculating the vertical-horizontal ($V-H$) failure envelope as well as the non-associated plastic potential surface. Zhang et al. (2002) defined the failure envelope shape as a generalisation of the envelope set out by Butterfield and Gottardi (1994):

$$H = \mu\,(V - V_{min})\,(1 - V/V_{max}) \tag{2}$$

where μ is a parameter controlling the gradient of the envelope at low V, V_{min} is the vertical uplift capacity and V_{max} is the purely vertical bearing capacity. This envelope implies that the maximum horizontal bearing capacity occurs at $V/V_{max} = 0.5$. Zhang et al. (2002) indicate that V_{max} is a function of pipeline embedment and is determined either from vertical load-penetration curves or estimated from the conventional vertical bearing capacity overburden factor, N_q, as:

$$V_{max} \approx k_{vp} w = \gamma' N_q w D \tag{3}$$

where k_{vp} is the gradient of the vertical bearing capacity increase with depth (units of kN/m/m). The friction parameter μ was suggested by Zhang et al. (2002) to be only a function of pipeline embedment:

$$\mu = 0.4 + 0.65w/D \tag{4}$$

based on calibration to their centrifuge data. Zhang et al. (2002) indicated that the model also provides reasonable fit to some of the silica sand results from the Verley and Sotberg (1994) database. However, the Zhang et al. (2002) model, like the Verley and Sotberg (1994) model, does not include any direct influence of soil friction angle or dilation angle (i.e. relative density) on the vertical bearing capacity or the horizontal breakout resistance at low vertical loads, other than that implied by Eq. 3.

Sandford (2012) conducted a set of experiments and non-associated flow finite element analyses of drained pipeline breakout in silica sand. Compared to Zhang et al. (2002), the overall response from the experiments and numerical analyses where of similar magnitude and produced similar envelope shapes but covered a limited range of soil properties and pipeline embedment levels. Beyond the work of Sandford (2012), the other published work to link drained pipeline bearing capacity to soil properties is by Gao et al. (2015), who presented a general slip-line solution for the ultimate drained vertical bearing capacity of pipelines. However, they did not consider the effect of non-associated flow on the response.

The previous work exploring pipeline breakout in sand (e.g. Verley and Sotberg 1994; Zhang et al. 2002; Sandford 2012) has not generalised the response to enable direct soil input to consider different friction and dilation angles or was focused on a limited range of soil properties and embedment levels. This paper expands upon the previous work by conducting non-associated flow finite element analyses (FEA) of the bearing capacity of shallowly embedded pipelines up to one diameter in embedment (w on Figure 1). The analyses cover a wider range of friction and dilation angles (i.e. relative density) than previously explored. The friction and dilation angles are consistently linked by the strength-dilatancy relationship presented by Bolton (1986). The results provide insight into scenarios when non-association is most important and in what scenarios simple limit analysis techniques with the use of a reduced friction angle accounting for non-association may be sufficiently accurate.

Bearing capacity on drained soil with non-associated flow

The non-associated flow of sands at failure has a significant effect on the limiting capacity of geotechnical systems (e.g. Drescher and Detournay 1993; Frydman and Burd 1997). For associated flow, plasticity theorems enable the bearing capacity of boundary value problems to be bounded uniquely for a given set of boundary conditions and failure criteria. However, for non-associated flow, these bounds are no longer valid, other than that the upper bound of an equivalent associated flow problem (i.e. same friction angle) also forms an upper bound on the solution of the non-associated problem (Davis 1968). The literature on non-associated flow analyses suggests that non-association introduces two primary consequences: (i) that bifurcation/localisation of failure planes results in non-uniqueness and (ii) a general reduction in the bearing capacity of the system as compared to associated flow. Bifurcation implies a switch from a homogeneous solution to the governing equations to a non-homogeneous (localised) one. Hence, a range of localised solutions to the governing equations are possible for non-associated flow problems (Krabbenhoft et al. 2012). In practice for numerical analyses, such non-uniqueness often manifests through sensitivity of the solution to mesh conditions and an irregular (unsteady) response in the limiting load with continuing displacement (e.g. Loukidis and Salgado 2009). By contrast, associated flow problems theoretically have a unique solution.

The second consequence of non-association is the general tendency for the load bearing capacity of the non-associated boundary value problem to be reduced as compared to an equivalent associated flow problem. This concept can be understood by analogy if one considers the sliding resistance of a rigid block with a purely frictional interface, or equivalently a direct shear test. In this case, the values of normal and shear stress acting on the horizontal interface do not necessarily lie on the plane of maximum obliquity to the Mohr's circle of stress (ϕ_{IF} on Figure 2), or in other words the operative friction angle on the horizontal plane may be less than the tangent friction angle. However, from the boundary constraints, lateral extension strain in the horizontal direction is zero. If it assumed that the directions of principal stress and principal strain increment are coaxial for soil undergoing plastic deformation (Roscoe 1970), Mohr's circles of stress and strain increment can be drawn as on Figure 2. The actual stresses acting on the interface plane can be determined from the Mohr's circles constructed on Figure 2 for a given set of Mohr-Coulomb soil properties and the dilation angle of the interface material. Noting that $sin(\phi_{MC}) = t/s$ and taking advantage of the sine rule to determine the interface friction angle, ϕ_{IF}, some rearrangement yields:

$$tan(\phi_{IF}) = \frac{sin(\phi_{MC})cos(\psi)}{1 - sin(\phi_{MC})sin(\psi)} \tag{5}$$

From Eq. 5, only when $\psi = \phi_{MC}$ does $\phi_{IF} = tan(\phi_{MC})$, so only under associated flow is the friction along a shear plane equal to the classical $tan(\phi_{MC})$ result. For $\psi < \phi_{MC}$, the friction ratio is lower - when $\psi = 0^o$, $tan(\phi_{IF}) = sin(\phi_{MC})$ as first shown by Hill (1950). These relations simply mean that within a soil continuum there exists some element on which the combination of $\tau/\sigma = tan(\phi_{MC})$ acts, but this stress ratio does not necessarily act on the shear plane itself.

Drescher and Detournay (1993) took advantage of this finding and proposed an approach to calculating the bearing capacity of a non-associated problem by using such modified material strength parameters within the framework of upper bound limit analysis. This enables a solution to be calculated that estimates the effect of non-association but cannot be a rigorous solution. The approach has been shown to provide reasonable estimates to various problems compared to finite element analyses (e.g. Michalowski and Shi 1995; Yin et al. 2001); however, Krabbenhoft et al. (2012) identified that, for certain problems, such as vertical uplift of buried anchors or pipelines, the use of modified parameters in an associated framework can overestimate the resistance. This is because the failure mechanism corresponding to associated flow can vary significantly from that of the non-associated case.

METHODOLOGY

Analysis software

The analyses described in this paper were performed using OptumG2, a commercially available finite element and finite element limit analysis software (OptumCE 2018). Associated flow analyses were conducted for both the upper and lower bound capacity using finite element limit analysis methods described by Lyamin and Sloan (2002a) and Lyamin and Sloan (2002b). OptumG2 incorporates adaptive remeshing procedures, which enable automated optimisation of failure mechanisms in terms of the size, position and orientation of the mesh elements. For non-associated flow analysis, elastoplastic finite element analysis was used with Mohr-Coulomb soil elements, as described in general terms briefly below.

Krabbenhoft et al. (2012) proposed a method for numerical analysis of non-associated flow problems that involves recasting the non-associated problem into variational form that can be solved using numerical procedures developed for associated flow problems. This recasting improves some of the numerical convergence issues reported for non-associated flow (e.g. Loukidis and Salgado 2009) and allows both the local strength (friction angle) and kinematic (dilation angle) criteria for a non-associated Mohr-Coulomb material, for example, to be satisfied at failure. For illustration purposes, a generalised failure criterion, $F(p)$, is first defined and converted to an algebraically equivalent form:

$$F(p) = q - Mp - k \tag{6}$$

$$\begin{aligned} F^*(p) &= q - Mp - k^*(p) \\ k^*(p) &= k + (M - N)p \end{aligned} \tag{7}$$

where p is the mean pressure, q is the deviatoric stress, M is some friction coefficient, N is some volumetric (dilation) coefficient, k is any true cohesion and k^* is a mean pressure-dependent apparent cohesion. Figure 3 illustrates the two failure criteria showing that the apparent cohesion (k^*) at a given instant is specified such that at the current mean stress level the same deviatoric stress at failure results from both Eq. 6 and Eq. 7. Applying the assumption of associated flow to these two failure criteria, the normal direction to Eq. 7 corresponds to the dilation coefficient and thus non-associated plastic flow at failure is achieved. From Eq. 7b, the mean stress is required to calculate k^*. Therefore, k^* must be explicitly calculated incrementally over a series of substeps for each calculation load increment. By using small substep increments, errors between F and F^* arising from differences in elastic and plastic stress states between the two can be minimised (Krabbenhoft et al. 2012). Explicit substep calculation of k^* allows its value to be known and F^* can then be used directly in implicit solution methods or solved in terms of variational principles. This approach does not alleviate the issue of bifurcation and localisation or non-uniqueness of solution. Therefore, use of such an approach remains approximate and should be compared with relevant experimental results.

Soil and pipeline parameter ranges

Analyses have been conducted for a range of pipeline embedment (w/D = 0.1, 0.2, 0.4, 0.6, 0.8 1.0) assuming a pipeline outer diameter of 1 m (although all results are presented non-dimensionally). In all cases, the pipeline was modelled as weightless (hence vertical load is applied to the pipeline as an independent variable and the results are presented in combined V-H space) and rigid; and pipe rotation is prevented during analysis. The pipeline was initially modelled as a polygon with a minimum side length of $0.1D$; however, the adaptive remeshing procedure locally refines the mesh in areas (including the pipeline perimeter) where more intense shearing occurs. This refinement achieved an approximately circular border at the pipe perimeter by the final remeshing step. The soil domain generally extended at least a distance of $3D$ on either side of the pipeline and $1.5D$ below the pipeline but was extended to minimise boundary effects when necessary. Figure 4 shows example refined meshes for associated and non-associated flow cases along with shear strain contours illustrating the failure mechanisms relevant for the two cases. The higher dilation angle of the associated flow case causes the shear zone to extend further forward from the pipe, leading to a larger passive wedge zone. Also, this dilatancy restricts the formation of a wedge behind the pipe that is visible for the non-associated case.

The soil was modelled as a cohesionless Mohr-Coulomb soil, with a constant effective unit weight of 10 kN/m^3 (noting again that the results are presented non-dimensionally). A Youngs modulus of 1000 MPa and a Poissons ratio of 0.3 were assumed for all analyses, although changing the stiffness value over the range 100 MPa to 1000 MPa produced a variation in limiting load for both associated and non-associated flow of less than 1.5%, which is consistent with the findings of Loukidis and Salgado (2009). The initial K_0 value for each analysis was based on the peak friction angle corresponding to Jakys equation, $K_0 = 1 - sin(\phi_{peak})$. The soil-pipeline interface condition was modelled as fully rough with the same soil properties as the surrounding material (the limitations of this assumption are discussed later).

Peak friction angles ranging from 25^o to 60^o for both associated and non-associated flow analyses are considered. For the non-associated analyses, variations in dilation angle are linked to peak friction angle following Bolton (1986), where $\psi = (\phi_{peak} - \phi_{cs})/0.8$, leading to the nine cases shown in Table 1. This range of friction and dilation angles is expected to cover a practical range of relevant soil properties and spans relative density from approximately 20% to 100%. Note that for the case of $\phi_{cs} = 45$ with the highest density a maximum value dilation angle of 18.75^o has been adopted instead of 25^o due to convergence issues for higher values.

Analysis approach

For associated flow limit analysis, a final mesh of 15,000 elements was adopted, with 4 remeshing iterations during each analysis. The high number of elements was adopted for associated flow analyses to achieve a targeted error between upper and lower bound results of 2%. If this criterion was not achieved, further adaptation steps were conducted to reduce the error, although in some cases at high friction angle the minimum achievable error was

10%. Associated flow results are presented as the average of the upper and lower bounds.

For non-associated flow finite element analysis, a mesh convergence study was first conducted by calculating the purely vertical bearing capacity of a pipeline on soil with properties, $\phi_{peak} = 45^o$ and $\psi = 25^o$, and varying the total number of elements in the model. In all cases, a total of 15 calculation steps were conducted for each analysis (5 elastic steps and 10 plastic steps), which was found to be sufficient based on sensitivity studies relative to adopting larger numbers of steps (i.e. larger numbers of calculation steps produced limited further refinement of the load averaged over the final 5 steps). Over these 15 calculation steps, the model was remeshed every three steps. Remeshing was conducted following the scheme described by Lyamin et al. (2005), where each remeshing involves three mesh refinement substeps utilising an initial 500 total elements (on the first substep) and subsequently increasing the number (and refining spatially) of the elements up to the final specified value. The pipeline embedment was varied from 0.1 to 1 D with total numbers of elements, after refinement, ranging from 1,000 to 6,000. The results of this study indicate that the difference in the calculated bearing capacity between cases with 3,000 and 6,000 elements is less than 5% (Figure 5), although notably the refinement curves are not monotonic due to the generally oscillatory load response. Therefore, 3,000 elements has been selected to provide a balance between computational cost and reasonable mesh convergence.

The bearing capacity envelopes under combined vertical-horizontal loading were determined by first calculating the uniaxial vertical downward and uplift bearing capacities. Further analyses are then conducted by applying a small initial constant vertical load to the pipeline (2 kN per unit length) and then applying 11 different combinations of horizontal and vertical load to failure, distributed between purely downward and purely upward. The small initial vertical load was applied to allow calculation of the failure envelope for analyses at very low failure vertical loads where the envelope intercept is $V \approx 0$. To provide additional detail of the envelope shape at low vertical load, further analyses were conducted by applying purely horizontal failure loads under constant vertical loads of 5 kN/m and 10 kN/m.

The presented limit loads are calculated as the average of the final 5 plastic load steps. Some analysis runs with large V/V_{max} did not reach a steady state, where for the final 5 steps the ratio of the mean plus standard deviation to the mean was less than 5%, within the standard number of loading increments. In this case, additional plastic steps were added until a steady oscillatory response was achieved. For some cases, particularly for $\phi_{peak} \geq 55^o$, this criteria was not able to be achieved, and results with oscillation ratios larger than 5% of the mean have generally been excluded from the envelope interpretations described later.

Dimensionless groups

The results are presented as dimensionless loads:

$$\overline{V} = \frac{V}{\gamma D^2}; \quad \overline{H} = \frac{H}{\gamma D^2} \tag{8}$$

To provide context to the relative ranges of $\overline{V}$ that apply in practice, it is useful to interpret $\overline{V}$ in terms of the pipeline specific gravity (SG), which is a commonly used terminology in pipeline engineering. The SG represents the effective self-weight of a pipeline (relative to water):

$$\overline{V} = \frac{V}{\gamma D^2} = \frac{\pi}{4}(SG - 1) \tag{9}$$

where SG is the specific gravity of the pipeline.

A pipe that is neutrally buoyant in water has $SG = 1$ meaning it applies zero vertical load to the seabed. Typical values of SG for gas pipelines and umbilical cables - which represent light and heavy extremes - are 1.2 and 3, which correspond to $\overline{V} = 0.2$ and 1.5 respectively. At the ends of a pipeline span, where the weight of the whole span is carried by a short length at the abutments, the vertical load may be increased by an order of magnitude. Similarly, when a pipe is laid on the seabed, the stress concentration at the touchdown point may increase $\overline{V}$ by a factor of 2-10, with higher values applying on stiff sandy soils. Even though the pipe in these analyses is modelled as weightless, the SG can be interpreted in terms of $\overline{V}$ either at the beginning of the breakout process (assuming no additional vertical loading due to spanning, for instance) or throughout the process, if a constant load path is considered.

Validation of analysis methodology

Figure 6 compares elastoplastic analysis in OptumG2 for vertically loaded, rough strip footings with previous numerical results for both associated (Martin 2003; Lyamin et al. 2007) and non-associated soils (Loukidis et al. 2008). The associated flow results are all within 5% of the previously reported values, and the calculated non-associated collapse loads are about 10% lower than the Loukidis et al. (2008) results. These comparisons suggest that: (a) the mesh and loading discretisation for the elastoplastic finite element analyses are appropriate given that the associated flow results are within a small margin of known solutions; and (b) the non-associated flow calculation approach and discretisation provides similar but lower bearing capacities compared to the Loukidis et al. (2008) results over a range of friction and dilation angles, as expected from the relatively higher mesh density utilised herein.

Two additional validations are provided by comparing results attained using the proposed analysis approach in OptumG2 with previously published pipeline bearing capacity analyses using an undrained Tresca model (Figure 7) or a non-associated Mohr-Coulomb model (Figure 8). Figure 7 compares limit analysis results with those by Martin and White (2012) for a fully rough pipeline interface with full tension allowed and a soil undrained strength of $\gamma D/s_u = 1$. The current results are generally within 5% of Martin and White (2012). Figure 8 compares with digitised results by Sandford (2012) for $w/D = 0.4$, which shows very good comparison across the range of ϕ_{peak} and ψ considered. Further confirmation of the appropriateness of the current approach for drained resistance can be found in Tom et al. (2017), where a similar approach is used with good success for back-calculating the uplift resistance of buried pipelines in relatively loose sand of known friction and dilation angles.

RESULTS

Vertical bearing capacity

Normalised vertical bearing capacity results are shown on Figure 9 for both the associated flow and non-associated flow cases up to a normalised embedment of 1.0. Upper bound estimates using a reduced friction angle (following Eq. 5) are also shown. Bearing capacity predictions from the recommendations of Zhang et al. (2002) as per Eq. 3 are shown for comparison, with N_q (Reissner 1924) calculated as:

$$N_q = e^{\pi tan(\phi)} tan\left(45^o + \frac{\phi}{2}\right)^2 \tag{10}$$

Eq. 10 estimates N_q values within 0.01% of exact values provided by Martin (2005).

The bearing capacity results generally increase slightly non-linearly with depth (i.e. the tangent stiffness reduces with depth). The results from limit analysis using Eq. 5 tend to underpredict the resistance compared to the non-associated flow results corresponding to the same combination of peak friction and dilation angles. This underprediction is particularly evident for high friction angles.

Using least-squares fitting, a power law relationship is fitted to the results with the corresponding fits also shown on Figure 9 following:

$$\overline{V}_{max} = A\left(\frac{w}{D}\right)^B \tag{11}$$

The fitted A coefficient for each analysis set, which represents $\overline{V}_{max}$ at $w/D = 1$, are plotted versus soil friction angle on Figure 10. The A coefficient increases with friction angle but the value at a given friction angle reduces with dilation angle. The coefficients on Figure 10 are grouped by the equivalent critical state friction angle. When grouped in this fashion, the results show consistent trends for each critical state friction angle. As a result, the following function has been fitted using least squares to the sets for each critical state friction angle (and to the associated flow as a separate fitting):

$$A = C_1 \left(e^{{\phi_{peak}}^{C_2}} \right)^{C_3 \phi_{peak}} \tag{12}$$

where C_1, C_2 and C_3 are additional fitting coefficients and angles are given in degrees.

Eq. 12 allows estimation of the A coefficient for various associated flow friction angles, as shown on Figure 10 using coefficients tabulated in Table 2, although the fit was weighted for friction angles less than 45^o and the values for higher friction angles are underpredicted. For non-associated flow, the C parameters are found to be linear functions of ϕ_{cs}, where a trend can be fitted by:

$$C_i = I_{c,i} + \phi_{cs} S_{c,i} \tag{13}$$

where C_i are the three C coefficients, $I_{c,i}$ is the fitted intercept at $\phi_{cs} = 0$ for each C_i as a function of ϕ_{cs} and $S_{c,i}$ is the slope of the C_i trend with ϕ_{cs}. Fitted values of $I_{c,i}$ and $S_{c,i}$ for each C_i are tabulated in Table 2 and shown on Figure 10.

The B coefficient shows less variation than A with respect to dilation angle and is primarily a function of ϕ_{peak}. Hence, a simple linear relationship to approximate this variation with peak friction angle is shown on Figure 11 corresponding to:

$$B = 1.3067 - 0.0123 \phi_{peak} \tag{14}$$

For small ϕ_{peak} the coefficient is close to unity, which corresponds to the vertical capacity increasing linearly with depth. As ϕ_{peak} increases, B reduces indicating that the tangential stiffness of vertical capacity reduces with depth.

The vertical bearing capacity results can be compared with experimental and numerical results presented by Sandford (2012), who presented a series of experiments investigating the vertical bearing capacity with embedment. Figure 12 shows the vertical bearing capacity measured in model experiments and the corresponding predictions based on Eq. 11 to

14 using the density information varying with depth as provided by Sandford (2012) and assuming the critical state friction angle to range from 34 to 38^o. Although the 36^o critical state angle appears to provide the best fit, this is slightly higher than the 34.3^o value reported by Sandford (2012). Nevertheless, the vertical response predictions compare reasonably well with the measured experimental data, given the uncertainties in measuring sand density and operative friction angle.

Overall failure envelope shape

Bearing capacities corresponding to different combinations of vertical and horizontal load vectors are presented on Figure 13 and 14 for 84 material and geometry combinations for associated and non-associated flow, respectively. Results are normalised by the maximum vertical bearing capacity, $\overline{V}_{max}$. For non-associated parameter combinations, portions of some envelopes are poorly defined for large values of $\overline{V}$ due to irregular load-displacement response and difficulties in achieving numerical convergence. This was particularly problematic for $\phi_{peak} \geq 55^o$, and hence some load cases are excluded from these results. Other than variability due to these issues, both sets of results indicate that the ratio $\overline{H}_{max}/\overline{V}_{max}$ increases with embedment and generally converges with increasing ϕ_{peak} or ψ. This trend means that for large ϕ_{peak} the vertical bearing capacity increases with embedment at a higher rate than the horizontal capacity.

Each envelope is also fitted (using a non-linear least squares approach) with a modified version of the envelope suggested by Zhang et al. (2002):

$$\frac{\overline{H}}{\overline{V}_{max}} = \mu * \left(\frac{\overline{V}}{\overline{V}_{max}} + \beta\right)^n * \left(1 - \frac{\overline{V}}{\overline{V}_{max}}\right)^m \tag{15}$$

where β represents the maximum vertical uplift (tension) capacity as a proportion of the maximum (downward) vertical capacity, μ is a constant proportional to $\overline{H}_{max}/\overline{V}_{max}$ for constant values of m and n, which are exponents that control envelope shape at low and high vertical loads, respectively.

Figures 15a and 15b show the variation in parameters n and m grouped by ϕ_{peak} as a function of w/D, where μ, n and m are all kept as independent variables in Eq. 15 (i.e. the fits corresponding to Figures 13 and 14) and β is taken directly as $|\overline{V}_{min}/\overline{V}_{max}|$. Parameter n increases slightly with w/D but generally falls within a relatively small range from approximately 0.5 to 0.8. Parameter m takes a larger range of values for the non-associated results with a slight increasing trend with ϕ_{peak}.

A simplified method of describing the trends in fitting parameters has been adopted to provide a first order approximation of the non-associated envelopes from these analyses. To implement this approach, we take advantage of the relatively small variation in n and the approximately linear relationship observed for m with respect to ϕ_{peak} - n is taken as a constant value corresponding to the mean of the non-associated results (i.e. 0.64) and m assumed to be:

$$m = 0.013\phi_{peak} + 0.4 \tag{16}$$

With these assumptions for n and m, Eq. 15 reduces to a two variable fitting problem for μ and β. Figure 16a shows the resulting fitted μ coefficients (with β assumed directly from the results) grouped by ϕ_{peak} as a function of w/D. There is a general trend, with some variation, of increasing μ with w/D and decreasing μ with ϕ_{peak}, which is qualitatively consistent with Figure 14. The resulting values of μ are fitted with a linear relationship via:

$$\mu = 0.2w/D + \mu_0 \tag{17}$$

where the slope 0.2 is assumed constant corresponding approximately to the slopes for $25^o \leq \phi_{peak} \leq 55^o$ and μ_0 is the intercept at $w/D = 0$. Figure 16b shows μ_0 as a function of ϕ_{peak}, which is also fit reasonably well by:

$$\mu_0 = -0.00437\phi_{peak} + 0.42 \tag{18}$$

Eq. 17 and 18 are similar to the relationship proposed by Zhang et al. (2002), except that μ_0 is a linear function of ϕ_{peak}, whereas in Zhang et al. (2002) it was taken as constant for the range of soils considered. Since only rough conditions have been considered in these analyses, the foregoing equations are relevant only for fully rough conditions, which is applicable for instance to most concrete weight coated pipelines in practice. Caution should therefore be taken applying these results to cases with smooth or intermediate roughness closer to smooth.

The resulting coefficients following Eq. 16-18 (and $n = 0.64$) allow envelopes to be inferred for different combinations of w/D and ϕ_{peak}. The appropriateness of this methodology can be seen by comparing the estimated values of $\overline{H}_{max}/\overline{V}_{max}$ with those calculated directly from the numerical results. Figure 17a shows non-associated $\overline{H}_{max}/\overline{V}_{max}$ calculated from Figure 14. Figure 17b compares $\overline{H}_{max}/\overline{V}_{max}$ using Eq. 16-18 with the values from Figure 17a. Good comparison is achieved using the relatively simple estimation relationship, which confirms that an approximation of the envelope shape and $\overline{H}_{max}/\overline{V}_{max}$ can be attained using this approach.

Low $\overline{V}/\overline{V}_{max}$ response

The previous section described the overall failure envelope response; however, the parameter space for practical applications is generally limited to a range of $\overline{V} < 10$, as described in Section 2. Furthermore, achieving a reasonable fit of Eq. 15 to the overall envelope does not provide sufficient accuracy to fit the results at small $\overline{V}/\overline{V}_{max}$, which converge more consistently than at larger $\overline{V}/\overline{V}_{max}$. Therefore, in this section the horizontal capacity results at small $\overline{V}/\overline{V}_{max}$ are presented directly, without an overall envelope fitting framework.

At small $\overline{V}/\overline{V}_{max}$, the horizontal bearing capacity is often defined by the ratio of horizontal to vertical load at failure - $\overline{H}/\overline{V}$. Figure 18 shows $\overline{H}/\overline{V}$ for $\overline{V} < 10$ for the considered parameter space. The non-associated results on Figure 18 indicate that $\overline{H}/\overline{V}$ increases with embedment, density (i.e. $\phi_{peak} - \phi_{cs} \approx \psi$) and ϕ_{cs} but reduces non-linearly as $\overline{V}$ increases.

Figure 18 also shows equivalent upper bound limit analysis results assuming a reduced friction angle following Eq. 5. These results show good comparison with the non-associated FEA results over the range of w/D and ϕ_{peak} considered. Also shown on Figure 18 are estimations due to a reinterpreted version of Eq. 4:

$$\frac{\overline{H}}{\overline{V}} = tan(\phi_{peak}) + \frac{1 + sin\,(\phi_{peak})}{1 - sin\,(\phi_{peak})}\frac{w}{D} \tag{19}$$

Eq. 19 comprises a superposition of frictional and passive resistance where the latter corresponds to a classical passive earth pressure multiplied by the pipeline embedment. This is similar to the relationship suggested by Zhang et al. (2002) for μ, except that soil ϕ_{peak} is a direct input and passive resistance varies with ϕ_{peak} instead of being solely a linear function of embedment. Similarly, the inclusion of soil strength properties in Eq. 19 also differentiates it from that suggested by Verley and Sotberg (1994), Eq. 1. As embedment increases, Eq. 19 does a reasonable job of estimating $\overline{H}/\overline{V}$ at very small $\overline{V}$, particularly for small ϕ_{peak} but underestimates the response increasingly as w/D and ϕ_{peak} increase. Eq. 19 also clearly cannot account for the variation in $\overline{H}/\overline{V}$ with $\overline{V}$.

The comparisons with simplified methods suggest that for relatively small values of $\overline{V}$, limit analysis with a reduced friction angle provides better prediction of the calculated non-associated resistances and captures the variation with $\overline{V}$. Good comparison is attained for small $\overline{V}$ load cases because the failure mechanism at these load levels is similar for both the associated and non-associated flow cases, which allows the associated flow approach suggested by Drescher and Detournay (1993) to reasonably capture the kinematics at failure. Comparison between the failure mechanisms is shown on Figure 19 along with comparison of failure envelopes for $\phi_{peak} = 45^o$, $\psi = 12.5^o$ for $w/D = 0.2$ and 0.8. The calculated bearing capacities are most disparate when the failure mechanisms differ most significantly. This comparison also reveals that the non-associated envelope at negative $\overline{V}$ is found to often be concave for $w/D > 0.5$, taking a heart shaped form with symmetry about the $\overline{V}$ axis. For the case of $w/D = 0.8$ on Figure 18, the vertical (uplift) bearing capacity component for at least two load vectors (160^o and 130^o) is higher than that for purely vertical loading. This response is common across the range of ϕ_{peak} and $\psi < \phi_{peak}$ considered. This is not necessarily surprising as although associated flow yield surfaces must conform to a convex shape (Drucker 1953), no such guarantee exists for non-associated flow.

Some insight into the origin of the relatively higher vertical capacities and the concavity of the failure envelope is gained by comparing the area of soil mobilized during breakout. There are two blocks of lifted soil, one on each side of the pipe (A_1 and A_2). The total lifted area is calculated as the volume of the two lifted soil blocks, $A_{soil} = A_1 + A_2$, and can be resolved into the vertical direction, A_{lift}, by factoring by $cos(\delta)$, where δ is the representative inclination of the individual block movements from the vertical (illustrated schematically on the insets on Figure 20). When resolved in this fashion, this quantity is akin to the work done by pipeline movement to lift the mobilized soil block. Figure 20a shows the variation in A_{lift}/D^2 with different load inclination angles (θ). As illustrated on Figure 20b, this quantity is somewhat proportional (but not exactly) to the resultant magnitude of the force vector at breakout. For associated flow, this quantity starts at a relatively large value for pure uplift (i.e. 0^o from vertical) and increases at a relatively slow rate with increasing loading angle. Hence, the resultant load magnitude increases relatively slowly compared to the loading angle and the envelope is convex. This shape occurs for associated flow because the area of soil lifted for pure uplift is similar to that for cases with non-zero loading angles, since the angles that the failure planes extend from the pipeline are approximately equal to ϕ_{peak}. For non-associated flow, the work due to the lifted soil increases more rapidly (relative to 0^o) over the first two steps in loading angle. From Figure 19 this is because of the larger increase in the soil volume within the failure mechanisms relative to the pure uplift case. This occurs because the failure planes extend from the pipeline at the small angle, ψ, and hence encompass much less soil in pure uplift loading for non-associated flow. However, the differences between associated and non-associated flow reduce with increasing loading angle as the mechanisms converge to become more similar.

APPLICATION AND LIMITATIONS

The results described herein have a few implications for design practice. First, for pipeline loading scenarios with predominantly vertical (upward or downward) loading trajectory, the pipeline breakout response can be reasonably described at low $\overline{V}/\overline{V}_{max}$ by directly utilising the results presented on Figure 18. Further, these results imply that one may be able to get very close agreement over this low $\overline{V}/\overline{V}_{max}$ range using upper bound limit analysis with a reduced friction angle to account for non-associated dilation following Eq. 5.

For relatively large values of $\overline{V}/\overline{V}_{max}$ or prediction of pipeline penetration, the reduced friction angle limit analysis approach is not recommended. For penetration predictions (or calculation of $\overline{V}_{max}$ to anchor the overall envelopes), Eqs. 11 through 14 and Figure 9 may be utilised to derive profiles of $\overline{V}_{max}$ with depth for given values of ϕ_{cs} and ψ. The workflow of such predictions is: (i) estimate ϕ_{cs} and ψ or ϕ_{peak} (possibly varying with depth); (ii) select B from Eq. 14 for the specified ϕ_{peak}; (iii) for a given ϕ_{cs} use Table 2 to calculate values of C_1, C_2 and C_3 from Eq. 13; (iv) calculate the A coefficient using Eq. 12 and inputs from (iii) for a given ϕ_{peak}; and (v) calculate the variation in $\overline{V}$ with depth using Eq. 11. This approach was shown to compare well with experimental results by Sandford (2012) on Figure 12.

To estimate the overall yield envelope shape, the normalised envelopes were found to be well described by Eq. 15. However, the coefficients to describe this envelope were found to vary somewhat, especially due to calculation difficulties at high $\overline{V}$. A first order approximation of estimating the overall envelope shape can be attained by using m calculated by Eq. 16, $n = 0.64$ as a constant, calculating μ via Eqs. 17 and 18 and choosing $\beta = 0$ for $w/D < 0.5$ and as approximately 0.05-0.1 following Zhang et al. (2002). This approach was shown to provide reasonable estimates of $\overline{H}_{max}/\overline{V}_{max}$ on Figure 17 but should not be utilised to predict the response accurately at low $\overline{V}$, since the parameter fitting was focused on capturing the overall shape.

The uplift resistance of pipelines with $w/D > 0.5$ is also poorly estimated by limit analysis due to the kinematic constraints imposed. This is primarily an issue for $\overline{V} < 0$, where the limit analysis approach may overestimate the resistance compared with the full finite element results. Fitted envelope results have not been provided for this range of $\overline{V}$, and hence caution should be taken when considering this range with inferred full envelopes as described above. If $\overline{V} < 0$ is of significant import for a practical problem, non-associated finite element analyses should be done with case-specific properties.

Additionally, there are a number of limitations to the present study that should be considered. First, the results focus only on a fully rough interface condition. Although this is relevant for many practical applications (for instance pipelines with concrete weight coat), the results are not directly applicable to smooth or intermediate roughness conditions. However, since limit analysis was shown to give good comparison over practical ranges of $\overline{V}$, it may also be inferred that use of a smooth interface in limit analysis would be able to reasonably capture the response in that scenario, although verifying this could be a useful extension of this work.

The current analyses are also predicated on the assumption of a wished-in-place and rigid pipeline. The first of these assumptions excludes explicit consideration of installation effects (such as heave and soil buoyancy). However, these effects are not believed to be as important for drained response as for the undrained behaviour (e.g. Merifield et al. 2009) because in the drained case penetration resistance due to shearing is significantly higher than for undrained conditions (at least for relatively soft clays where heave is important). Moreover, the good comparison attained between the present wished-in-place assumption results and the experimental results of Sandford (2012) corroborates this conclusion. Nevertheless, a useful future extension of this work could be to consider installation effects, for instance, through large deformation analyses. The rigid pipeline assumption means that the results are directly relevant when steel or concrete pipelines are utilised, although a rigid pipeline assumption is typically adopted as standard practice in the offshore industry.

CONCLUSIONS

This paper describes a series of finite element and limit analysis results describing the effects of non-associated flow, and by inference soil density, on the bearing capacity of shallowly embedded pipelines. The analyses cover a range of soil parameters relevant for practical application. Due to inherent non-uniqueness in analysis of non-associated materials, these results form only one particular solution to each considered scenario. However, the results compare favourably with other numerical results available in the literature as well as the limited experimental data that exists in the public domain with sufficient soils information to enable reasonable comparison. Therefore, some conclusions can be made from these results towards improving the current state of pipeline engineering practice.

The vertical bearing capacity was found to be strongly affected by non-association and using a reduced friction angle within a limit analysis framework does not appear to provide a satisfactory method to account for this. The increase with depth was found to consistently follow a power law relationship that is approximately linear at small ϕ_{peak} and becomes non-linear (with a power reducing less than unity) with increasing ϕ_{peak}. A series of relationships to predict the variation in vertical bearing capacity for given combinations of ϕ_{cs} and ψ have been provided, which provide good comparison with the experimental results of Sandford (2012).

The overall shape of the combined V-H loading envelopes was found to be similar to that described previously by Zhang et al. (2002) but with the peak horizontal load occurring at a relatively smaller proportion of the maximum vertical bearing capacity. The calculated values of maximum horizontal load were found to generally increase with embedment as a proportion of the maximum vertical bearing capacity. As friction angle increases, the rate of increase in $\overline{H}_{max}/\overline{V}_{max}$ reduces because the vertical bearing capacity increases at a faster rate with friction angle than the horizontal bearing capacity. A modified version of the envelope suggested by Zhang et al. (2002) was shown to fit to the analysis results well, and a simplified methodology for first order predictions of the overall envelope shape have been provided.

The response at small values of vertical load have been interpreted in terms of the variation in the ratio $\overline{H}/\overline{V}$ with $\overline{V}$. For loading scenarios with a predominantly horizontal load component, the effect of non-association is well predicted by using a reduced friction angle in limit analysis. This is a useful practical finding, given that increasing density results in much larger values of $\overline{H}/\overline{V}$ relative to critical state conditions for the same embedment level, because this indicates that relatively simple limit analysis calculations may be used to describe the variation in response for practical scenarios with different, site-specific seabed geometries.

Finally, it was also found that the shape of the non-associated flow envelopes for $w/D >$ 0.5 can be concave in the region of near-vertical uplift. This is linked to the differences in the area of soil mobilised during loading at these angles.

ACKNOWLEDGEMENTS

This work was funded by research and development grants from the University of Western Australia (UWA) and the ARC Industrial Transformation Research Hub for Offshore Floating Facilities, which is funded by the Australian Research Council, Woodside Energy, Shell, Bureau Veritas and Lloyds Register (Grant No. IH140100012). The authors would also like to thank Scott Draper for helpful comments during the preparation of this paper.

REFERENCES

Bolton, M. (1986). "The strength and dilatancy of sands." *Géotechnique*, 36(1), 65–78.

Butterfield, R. and Gottardi, G. (1994). "A complete three-dimensional failure envelope for shallow footings on sand." *Géotechnique*, 44(1), 181–184.

Davis, E. (1968). "Theories of plasticity and failures of soil masses." *Soil mechanics, selected topics.*

Drescher, A. and Detournay, E. (1993). "Limit load in translational failure mechanisms for associative and non-associative materials." *Géotechnique*, 43(3), 443–456.

Drucker, D. C. (1953). “Coulomb friction, plasticity, and limit loads.” *Report no.*, Brown University.

Frydman, S. and Burd, H. J. (1997). “Numerical studies of bearing-capacity factor n γ.” *Journal of geotechnical and geoenvironmental engineering*, 123(1), 20–29.

Gao, F.-P., Wang, N., and Zhao, B. (2015). “A general slip-line field solution for the ultimate bearing capacity of a pipeline on drained soils.” *Ocean Engineering*, 104, 405–413.

Hill, R. (1950). *The mathematical theory of plasticity*, Vol. 11. Oxford university press.

Krabbenhoft, K., Karim, M., Lyamin, A., and Sloan, S. (2012). “Associated computational plasticity schemes for nonassociated frictional materials.” *International Journal for Numerical Methods in Engineering*, 90(9), 1089–1117.

Loukidis, D., Chakraborty, T., and Salgado, R. (2008). “Bearing capacity of strip footings on purely frictional soil under eccentric and inclined loads.” *Canadian Geotechnical Journal*, 45(6), 768–787.

Loukidis, D. and Salgado, R. (2009). “Bearing capacity of strip and circular footings in sand using finite elements.” *Computers and Geotechnics*, 36(5), 871–879.

Lyamin, A., Salgado, R., Sloan, S., and Prezzi, M. (2007). “Two-and three-dimensional bearing capacity of footings in sand.” *Géotechnique*, 57(8), 647–662.

Lyamin, A. and Sloan, S. (2002a). “Lower bound limit analysis using non-linear programming.” *International Journal for Numerical Methods in Engineering*, 55(5), 573–611.

Lyamin, A. V. and Sloan, S. (2002b). “Upper bound limit analysis using linear finite elements and non-linear programming.” *International Journal for Numerical and Analytical Methods in Geomechanics*, 26(2), 181–216.

Lyamin, A. V., Sloan, S. W., Krabbenhft, K., and Hjiaj, M. (2005). “Lower bound limit analysis with adaptive remeshing.” *International Journal for Numerical Methods in Engineering*, 63(14), 1961–1974.

Martin, C. (2003). “New software for rigorous bearing capacity calculations.” *Proc. int. conf. on foundations*, 581–592.

Martin, C. (2005). "Exact bearing capacity calculations using the method of characteristics." *Proc. IACMAG. Turin*, 441–450.

Martin, C. and White, D. (2012). "Limit analysis of the undrained bearing capacity of offshore pipelines." *Géotechnique*, 62(9), 847–863.

Merifield, R. S., White, D. J., and Randolph, M. F. (2009). "Effect of surface heave on response of partially embedded pipelines on clay." *Journal of Geotechnical and Geoenvironmental Engineering*, 135(6), 819–829.

Michalowski, R. L. and Shi, L. (1995). "Bearing capacity of footings over two-layer foundation soils." *Journal of Geotechnical Engineering*, 121(5), 421–428.

OptumCE (2018). *OptumG2*, <http://optumce.com/>.

Reissner, H. (1924). "Zum erddruckproblem." *1st Int. Congress for Applid Mechanics*.

Roscoe, K. H. (1970). "The influence of strains in soil mechanics." *Géotechnique*, 20(2), 129–170.

Sandford, R. J. (2012). "Lateral buckling of high pressure/high temperature on-bottom pipelines." Ph.D. thesis, University of Oxford, Oxford, United Kingdom.

Tom, J., O'Loughlin, C., White, D., Haghighi, A., and Maconochie, A. (2017). "The effect of radial fins on the uplift resistance of buried pipelines." *Géotechnique Letters*, 7(1), 60–67.

Verley, R. and Sotberg, T. (1994). "A soil resistance model for pipelines placed on sandy soils." *Trans. ASME Jour. Offshore Mechanics and Arctic Engineering*, 116, 145–153.

Yin, J. H., Wang, Y. J., and Selvadurai, A. (2001). "Influence of nonassociativity on the bearing capacity of a strip footing." *Journal of geotechnical and geoenvironmental engineering*, 127(11), 985–989.

Zhang, J. (2001). "Geotechnical stability of offshore pipelines in calcareous sand." Ph.D. thesis, University of Western Australia, Perth, Australia.

Zhang, J., Stewart, D. P., and Randolph, M. F. (2002). "Modeling of shallowly embedded offshore pipelines in calcareous sand." *Journal of geotechnical and geoenvironmental engineering*, 128(5), 363–371.

List of Tables

TABLE 1

Adopted friction and dilation angle parameter sets

Critical state friction angle ϕ_{cs} (^{o})		$\phi_{peak} - \phi_{cs}$ (^{o})		
		0	10	20
25	ϕ_{peak} (^{o})	25	35	45
	ψ (^{o})	0	12.5	25
35	ϕ_{peak} (^{o})	35	45	55
	ψ (^{o})	0	12.5	25
45	ϕ_{peak} (^{o})	45	55	60
	ψ (^{o})	0	12.5	18.75*

Note*: 18.75^o has been adopted instead of 25^o due to convergence issues.

TABLE 2

Fitted coefficients for vertical capacity (Eq. 12)

<table>
<tr><th colspan="3">Coefficient</th><th>Value</th></tr>
<tr><td rowspan="3">Associated flow</td><td colspan="2">C_1</td><td>4.95</td></tr>
<tr><td colspan="2">C_2</td><td>1.22</td></tr>
<tr><td colspan="2">C_3</td><td>8.36×10^{-4}</td></tr>
<tr><td rowspan="6">Non-Associated flow</td><td rowspan="2">C_1</td><td>$S_{c,1}$</td><td>0.07</td></tr>
<tr><td>$I_{c,1}$</td><td>1.75</td></tr>
<tr><td rowspan="2">C_2</td><td>$S_{c,2}$</td><td>0.0163</td></tr>
<tr><td>$I_{c,2}$</td><td>0.6467</td></tr>
<tr><td rowspan="2">C_3</td><td>$S_{c,3}$</td><td>-5.97×10^{-5}</td></tr>
<tr><td>$I_{c,2}$</td><td>0.0030</td></tr>
</table>

List of Figures

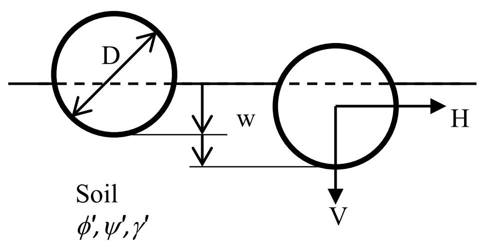

Fig. 1. Problem definition.

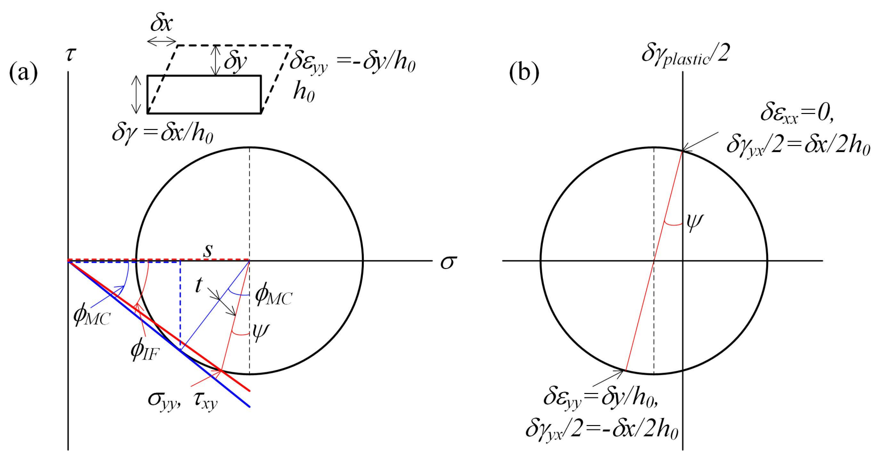

Fig. 2. Mohr's circle of (a) stress and (b) strain rate at failure.

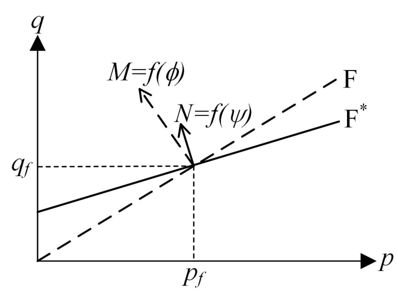

Fig. 3. Frictional Mohr-Coulomb failure criteria unmodified F (Eq. 6) and modified for substepping F^* (Eq. 7).

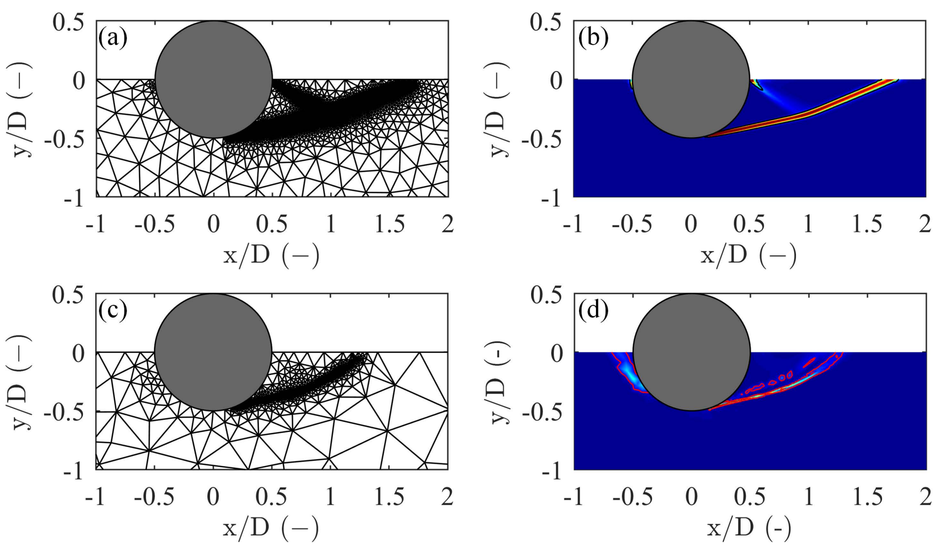

Fig. 4. Example refined meshes (a and c) and shear strain contours (b and d) for $\overline{V} = 0.5$. Associated Flow, $\phi = 45^o$, $N_{elem} = 15,000$: (a) refined mesh; (b) shear strain at failure, blue: low, red: high. Non-associated flow, $\phi_{peak} = 45^o$, $\psi = 12.5^o$, $N_{elem} = 3,000$: (c) refined mesh; (d) shear strain at failure, blue: low, red: high.

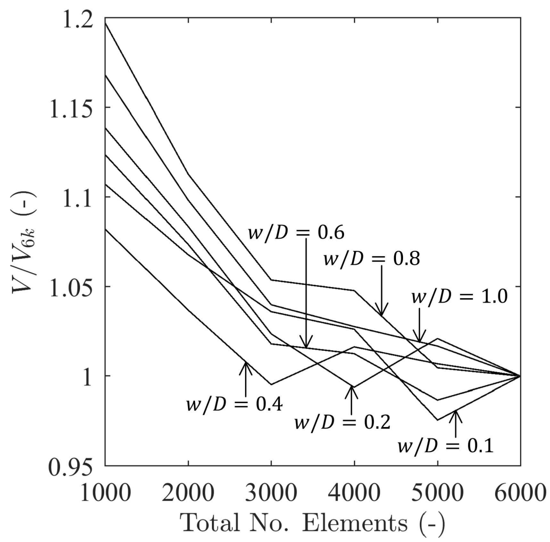

Fig. 5. Sensitivity of vertical bearing capacity with total number of elements. $\phi_{peak} = 45^o$, $\psi = 25^o$.

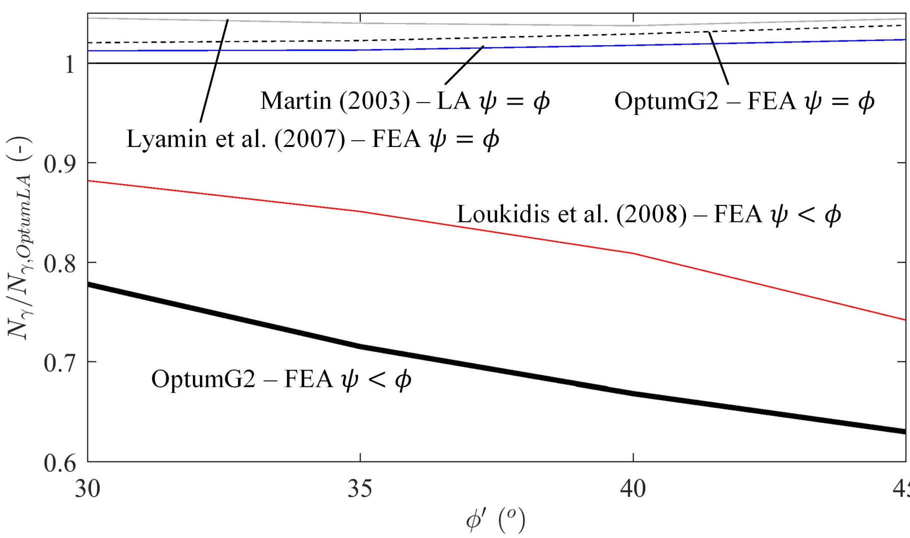

Fig. 6. Comparison of vertical bearing capacity factors for strip footing with previously published results.

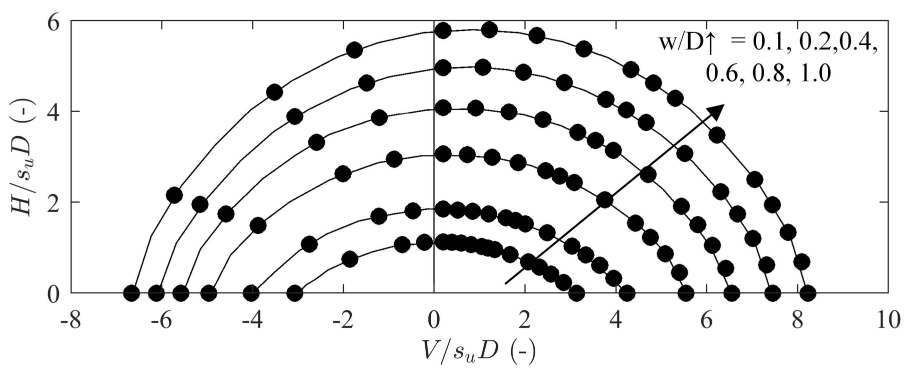

Fig. 7. Comparison of undrained $V-H$ envelopes with Martin and White (2012) for $\gamma D/s_u = 1$. Solid circles - current analysis. Black lines - Martin and White (2012).

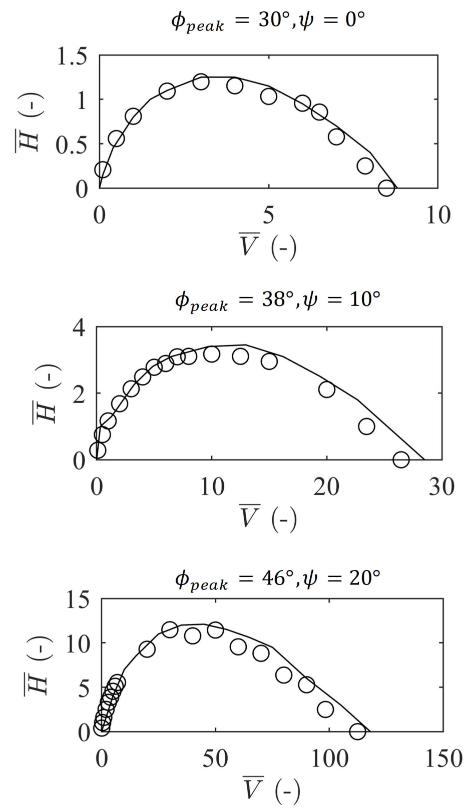

Fig. 8. Comparison of drained $V - H$ envelopes with Sandford (2012) for $w/D = 0.4$. Solid circles - current analysis. Black lines - Sandford (2012).

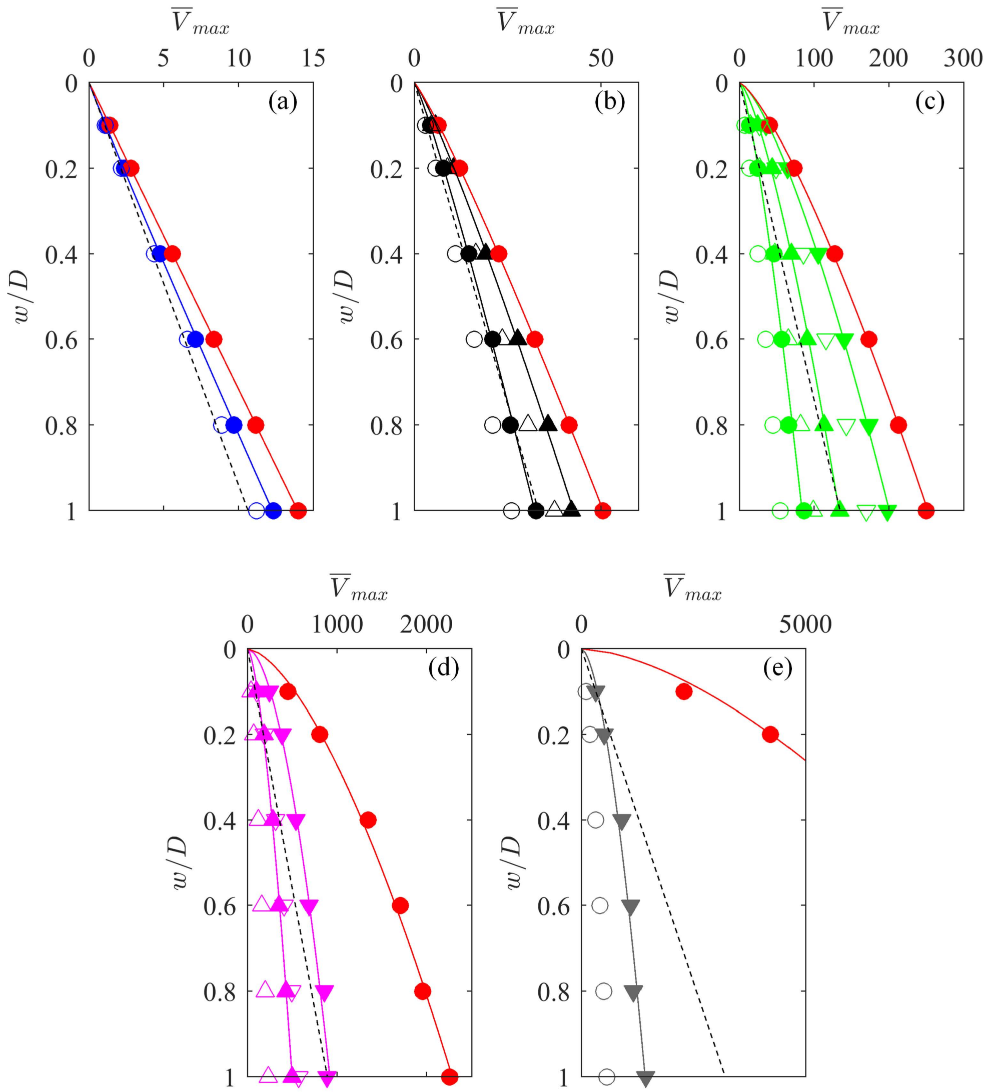

Fig. 9. $\overline{V}_{max}$ variation with embedment depth. Solid symbols - non-associated flow results. Open symbols - associated flow results using reduced friction angle as per Eq. 5. Solid red circles - associated flow results with specified ϕ_{peak}. Dashed lines - prediction with Eq. 3 and 10. Solid lines - power law fits to current results. (a) $\phi_{peak} = 25^o$. (b) $\phi_{peak} = 35^o$. (c) $\phi_{peak} = 45^o$. (d) $\phi_{peak} = 55^o$. (e) $\phi_{peak} = 60^o$.

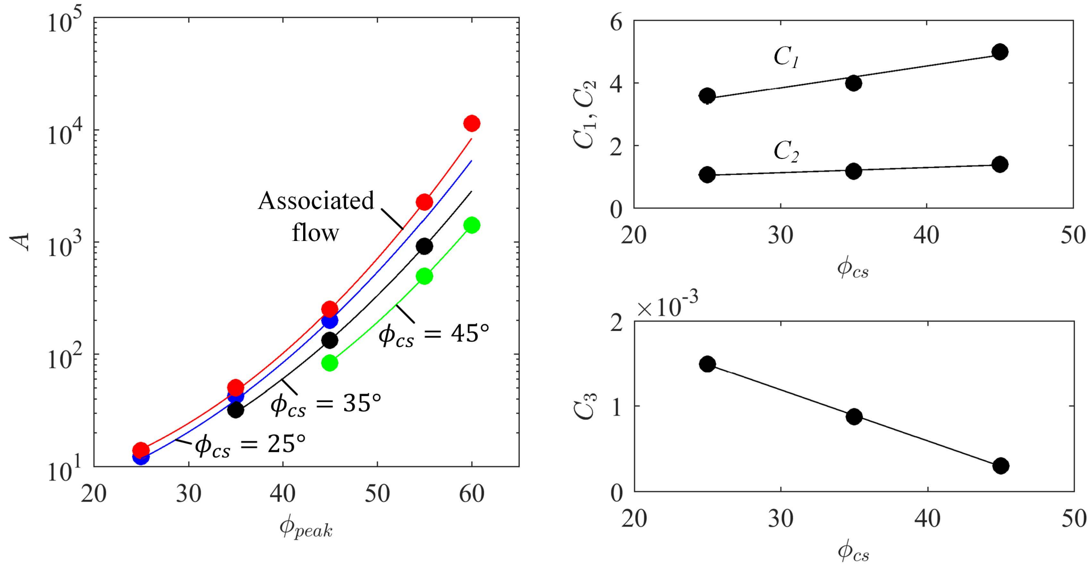

Fig. 10. Variation in A coefficient and C coefficients with friction angle (note: relationships for C coefficients are based on critical state friction angle; Eq. 12 function for A coefficient is based on peak friction angle).

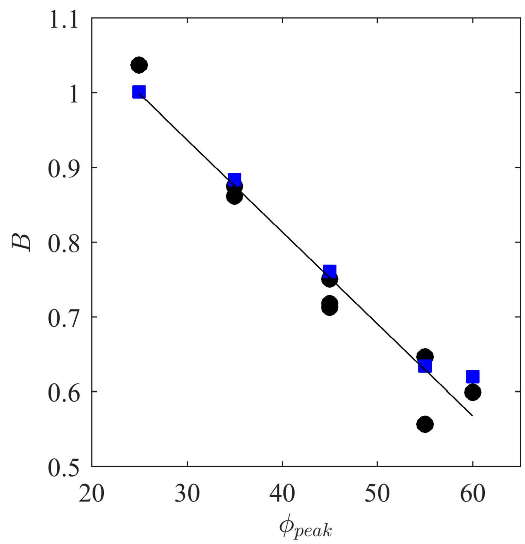

Fig. 11. Variation in B coefficient with ϕ_{peak}. Black Circles - non-associated flow. Blue squares - associated flow.

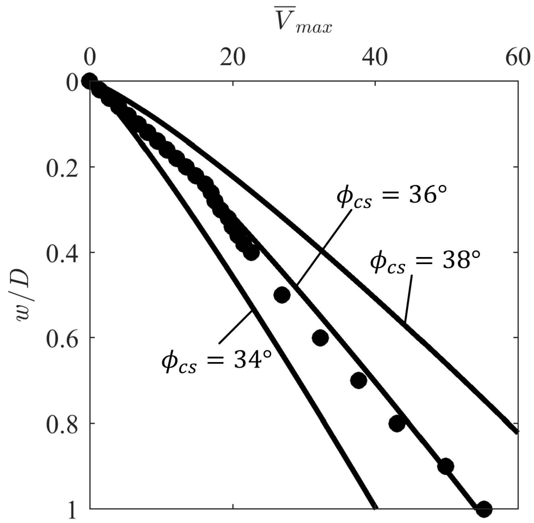

Fig. 12. Vertical penetration response, assuming relative density of 20%, compared with experimental results from Sandford (2012). Solid lines - predictions based on Eq. 11 to 14. Solid circles - values reproduced from Sandford (2012).

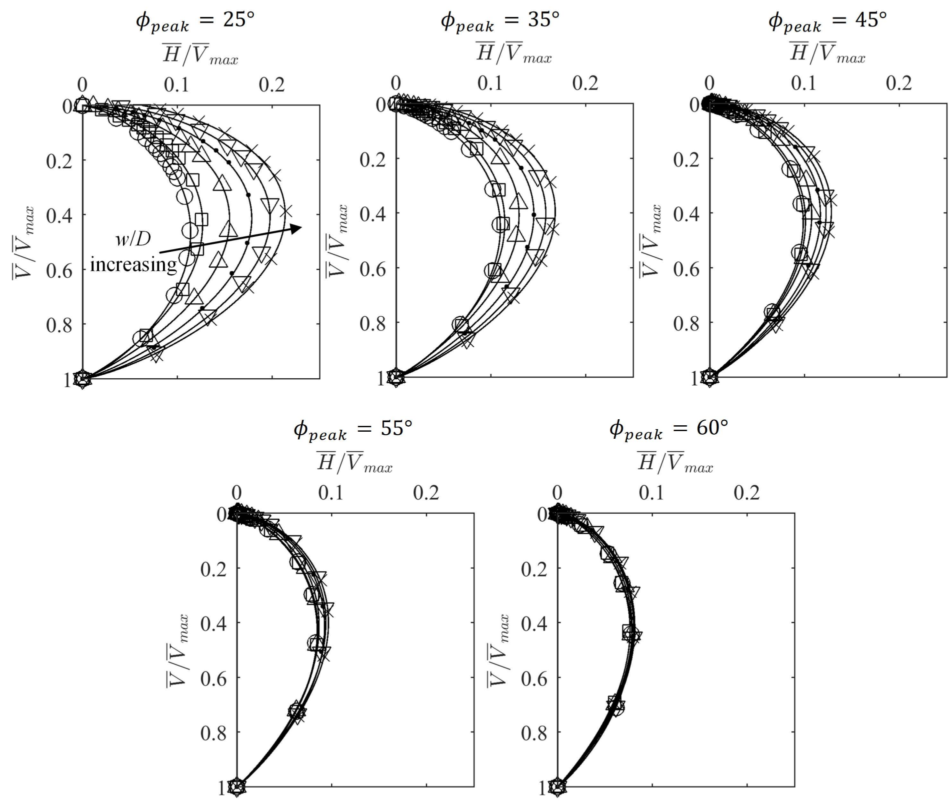

Fig. 13. Combined loading failure envelopes for the associated flow sets. Circles - $w/D = 0.1$. Squares - $w/D = 0.2$. Upward triangles - $w/D = 0.4$. Dots - $w/D = 0.6$. Downward triangles - $w/D = 0.8$. Crosses - $w/D = 1.0$. Lines - fitted envelopes based on least squares to Eq. 15.

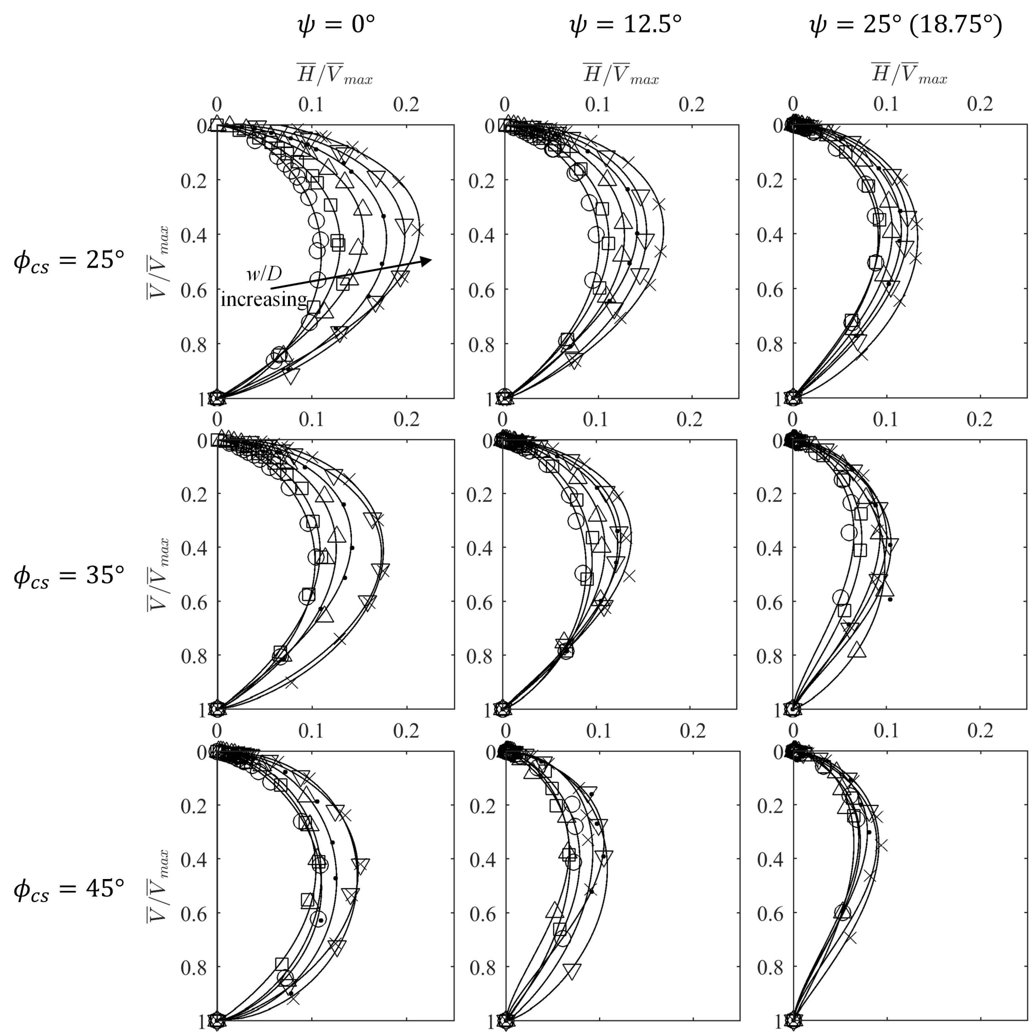

Fig. 14. Combined loading failure envelopes for the non-associated flow sets. Circles - $w/D = 0.1$. Squares - $w/D = 0.2$. Upward triangles - $w/D = 0.4$. Dots - $w/D = 0.6$. Downward triangles - $w/D = 0.8$. Crosses - $w/D = 1.0$. Lines - fitted envelopes based on least squares to Eq. 15.

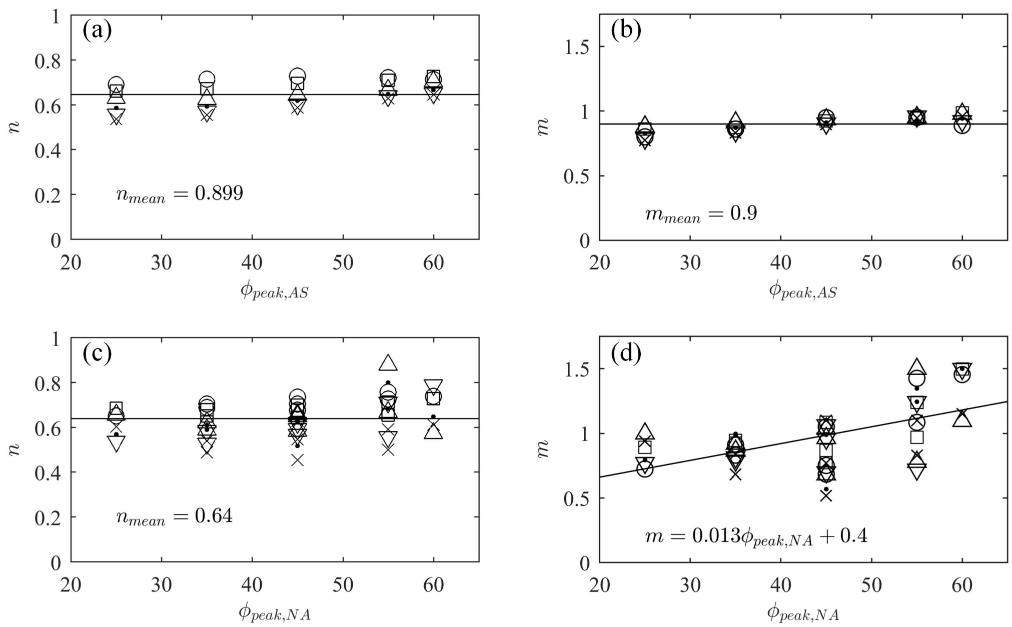

Fig. 15. Fitted n and m coefficients for Eq. 15 for (a) n coefficient - associated flow. (b) m coefficient - associated flow. (c) n coefficient - non-associated flow. (d) m coefficient - non-associated flow. Circles - $w/D = 0.1$. Squares - $w/D = 0.2$. Upward triangles - $w/D = 0.4$. Dots - $w/D = 0.6$. Downward triangles - $w/D = 0.8$. Crosses - $w/D = 1.0$.

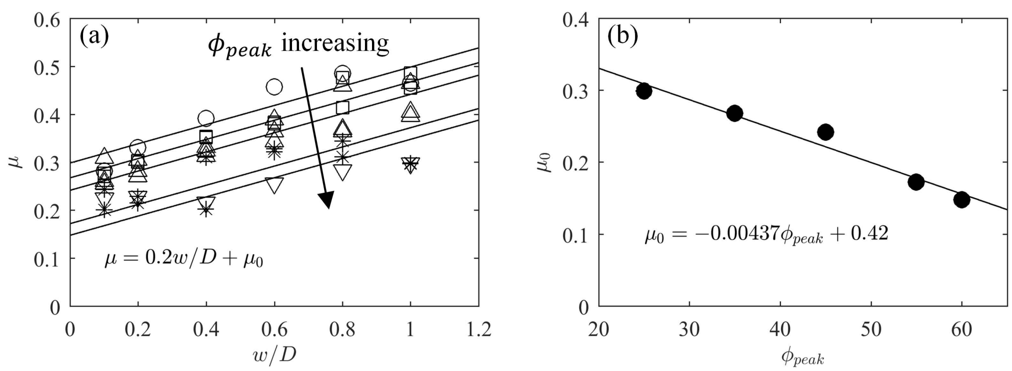

Fig. 16. Fitted μ coefficients based on fitted values of n and m as per non-associated results on Figure 15. (a) Fits to numerical results. Circles - $\phi_{peak} = 25^o$. Squares - $\phi_{peak} = 35^o$. Upward triangles - $\phi_{peak} = 45^o$. Asterisks - $\phi_{peak} = 55^o$. Downward triangles - $\phi_{peak} = 60^o$. (b) Intercept to linear fits to μ_0.

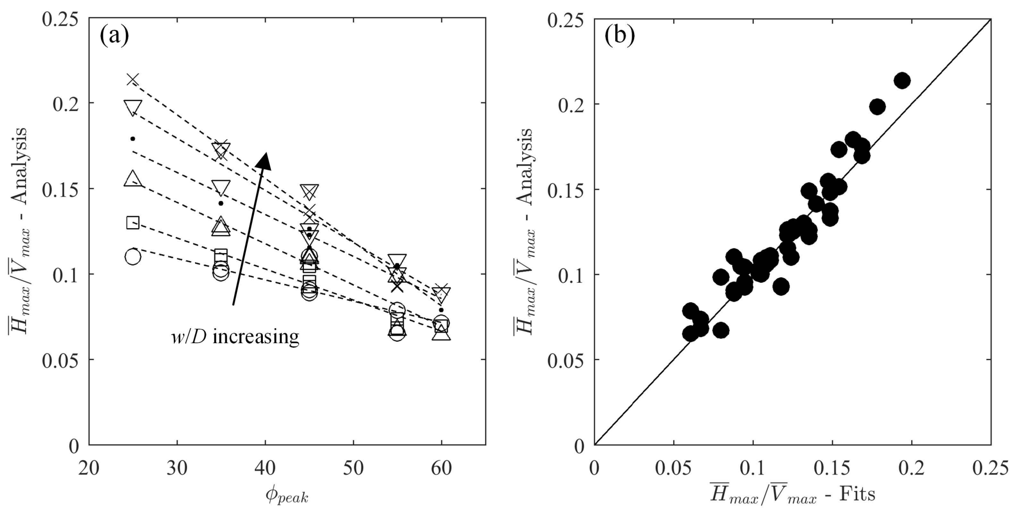

Fig. 17. Maximum normalised horizontal load. (a) Trends from non-associated numerical results. Circles - $w/D = 0.1$. Squares - $w/D = 0.2$. Upward triangles - $w/D = 0.4$. Dots - $w/D = 0.6$. Downward triangles - $w/D = 0.8$. Crosses - $w/D = 1.0$. (b) Comparison of numerical results with values derived from Figures 15-16.

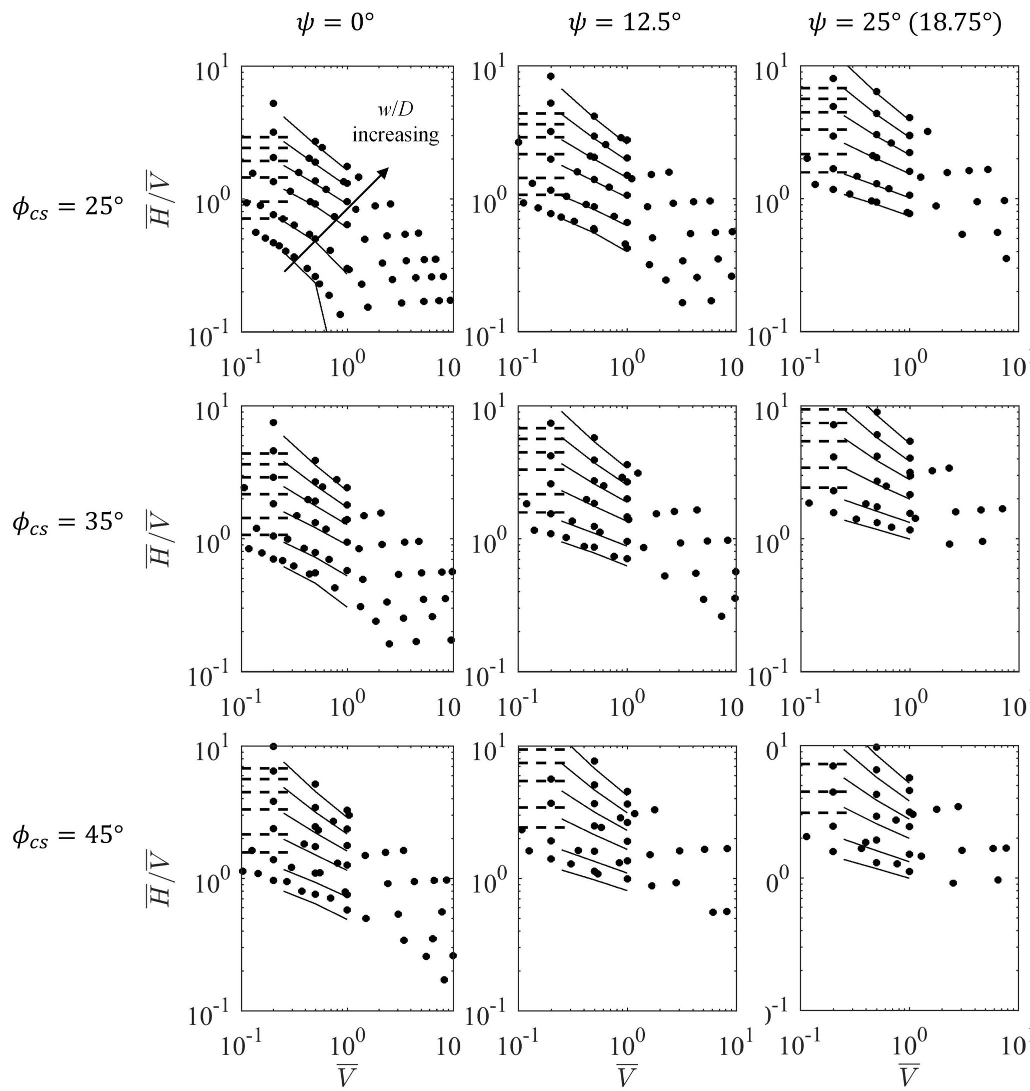

Fig. 18. Ratio of $\overline{H}/\overline{V}$ at failure. Solid circles - non-associated flow results. Solid lines - associated flow results using reduced friction angle as per Eq. 5. Dashed lines - Eq. 19.

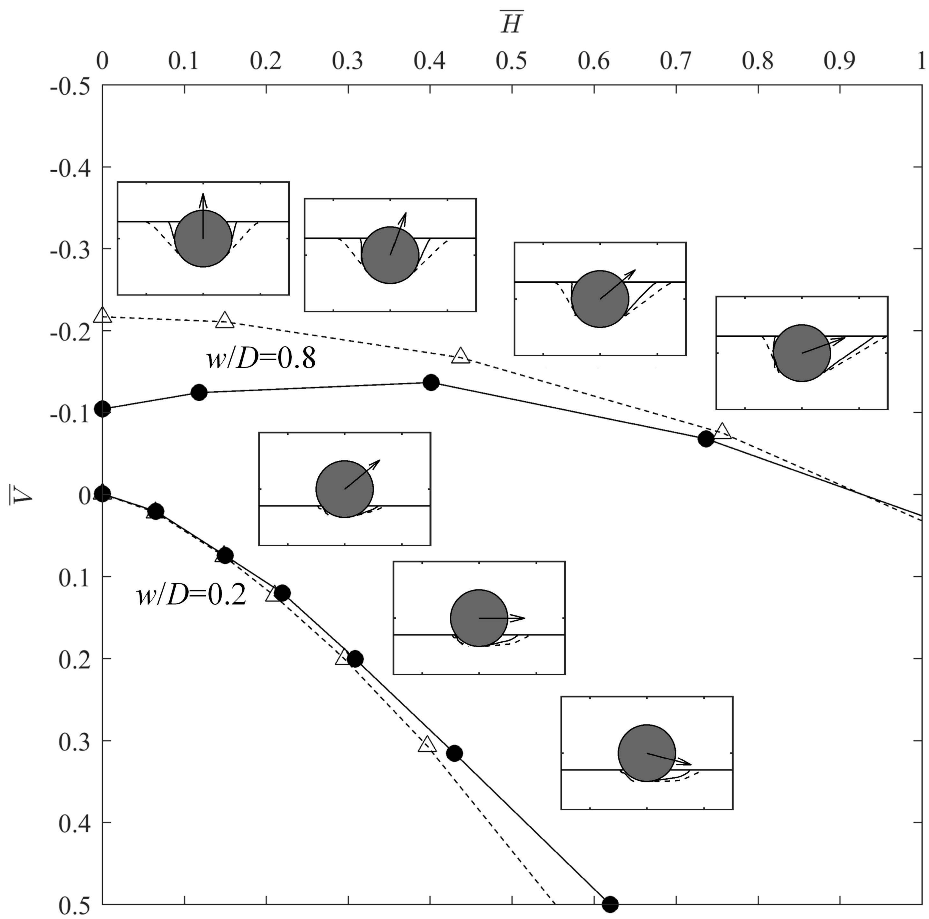

Fig. 19. Example low $\overline{V}$ results highlighting uplift component and displacement mechanisms. $\phi_{peak} = 45^o$, $\psi = 12.5^o$ for $w/D = 0.2$ and 0.8. Solid lines - non-associated FEA. Dashed lines - associated flow limit analysis with friction angle as per Eq. 5.

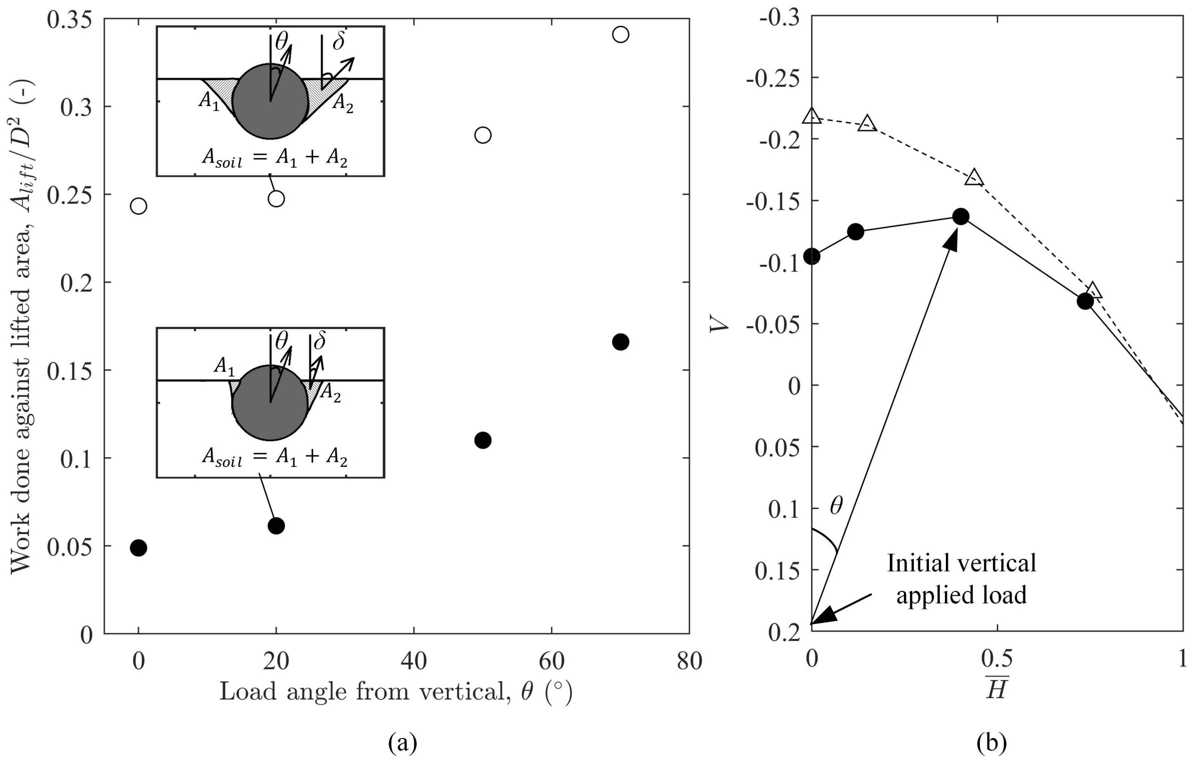

Fig. 20. Work done to lift mobilised soil area. (a) Variation in normalised work with load angle (note that the illustrated δ values are schematic); (b) Definition of loading angle. $\phi_{peak} = 45^o$, $\psi = 12.5^o$ for $w/D = 0.8$. Solid symbols - non-associated FEA. Open symbols - associated flow limit analysis with friction angle as per Eq. 5.